A Sensitivity Analysis on 3D Velocity Reconstruction from Multiple Registered Echo Doppler Views

Alberto Gomez[a,*], Kuberan Pushparajah[b,a], John M. Simpson[b,a], Daniel Giese[a], Tobias Schaeffter[a], Graeme Penney[a]

[a] *Division of Imaging Sciences and Biomedical Engineering, King's College of London, UK*
[b] *Guy's and St Thomas' Hospital, London, UK*

Abstract

We present a new method for reconstructing a 3D+t velocity field from multiple 3D+t colour Doppler images. Our technique reconstructs 3D velocity vectors from registered multiple standard 3D colour Doppler views, each of which contains a 1D projection of the blood velocity. Reconstruction is based on a scalable patch-wise Least Mean Squares approach, and a continuous velocity field is achieved by using a B-spline grid.

We carry out a sensitivity analysis of clinically relevant parameters which affect the accuracy of the reconstruction, including the impact of noise, view angles and registration errors, using simulated data. A realistic simulation framework is achieved by a novel noise model to represent variations in colour Doppler images based on multiscale additive Gaussian noise. Simulations show that, if the Target Registration Error $< \mathbf{2.5}\boldsymbol{mm}$, view angles are $> \mathbf{20°}$ and the standard deviation of noise in the input data is $< \mathbf{10}\boldsymbol{cm/s}$, the reconstructed velocity field presents visually plausible flow patterns and mean error in flow rate is approximately **10%** compared to 2D+t Flow MRI. These results are verified by reconstructing 3D velocity on 3 healthy volunteers. The technique is applied to reconstruct 3D flow on three paediatric patients showing promising results for clinical application.

Keywords: Colour Doppler Echocardiography, 3D Velocity Reconstruction, Flow Patterns, Multiple Views, Image Registration

1. Introduction

Many cardiac conditions are characterised by abnormalities of blood flow including regurgitation and narrowing of heart valves resulting in abnormal direction and velocity. Accurate 3D characterisation, quantification and visualisation of cardiac blood flow remains a challenge but has the potential to improve diagnosis of some cardiac diseases (Sengupta et al., 2012). In addition, 3D velocity information could be useful input to help constrain and validate patient specific cardiac models.

Latest advances in temporally resolved 3 directional flow-encoded 3D MRI (3D+t Flow MRI) over the past years have enabled non-invasive measurements of 3D velocities within the cardiovascular system. However, MRI is more expensive, requires long acquisition times compared to echocardiography (echo), and is incompatible with a number of cardiac implants such as pacemakers. In addition,

*Corresponding author. Address: Alberto Gomez, Division of Imaging Sciences and Biomedical Engineering, The Rayne Institute, 3th Floor, Lambeth Wing, St Thomas' Hospital, London SE1 7EH, UK.
Email address: alberto.gomez@kcl.ac.uk

transthoracic echo examinations are carried out 75 times more often than cardiac Magnetic Resonance Imaging (MRI) (Tsai-Goodman et al., 2004), which means that cardiac MRI is used on selected patients only, and always after an echo exam.

The recent introduction of 2D matrix array echo technology allows rapid acquisition of 3D B-Mode and 3D colour Doppler volumes. Nevertheless, Doppler velocity information is only a 1D projection of the true 3D velocity vector along the echo beam direction.

Crossed-beam techniques, which use multiple views to reconstruct the full velocity information, have the potential to overcome this limitation (Dunmire et al., 2000). One of the first crossed-beam approaches, proposed by Fox (1978), used simultaneous acquisition of several 2D Doppler images to compute an instantaneous 3D laminar flow on a 1D line. Xu et al. (1991) reconstructed 2D flows using more than two views, and improved reconstruction quality using two averaging methods. Recent work by Garcia et al. (2010) proposed the computation of 2D intraventricular flow using one colour Doppler image and boundary conditions from wall motion estimation. Uejima et al. (2010) proposed a method to compute 2D intraventricular velocity fields by splitting the flow field into a base field and a turbulence field using a single 2D colour Doppler image. In both the work by Garcia et al. (2010) and Uejima et al. (2010) the extension to 3D is not trivial since they both rely on the linear separability of the 2D continuity equation in polar coordinates. Unfortunately, separation of variables cannot be applied to the 3D version of the continuity equation in spherical coordinates. Arigovindan et al. (2007) proposed to use 2D B-splines and regularisation to reconstruct smooth 2D blood velocities in the carotid bifurcation and 2D tissue motion in the myocardium.

To our knowledge previous approaches have only reconstructed 2D projections of the true underlying 3D flow (Sengupta et al., 2012). However, blood flow patterns may be complex 3D patterns and their 2D projection provides only a part of the flow information. In addition, quantification of flow with 1D and 2D velocity maps requires correct alignment of the image and the plane of interest during acquisition. An accurate 3D velocity map would allow retrospective flow quantification through arbitrary planes, *i.e.* planes at the location of interest with an arbitrary orientation.

We propose to reconstruct the 3D velocity field on a regular 3D B-spline grid. This, to our knowledge, is the first time a full 3D velocity field has been reconstructed from Doppler images. Our method is a reformulation of the 2D method proposed by Arigovindan et al. (2007). Extension of this method to 3D is more complex due to both algorithmic and data acquisition reasons. On the algorithmic side: reconstruction of velocity vectors in 3D instead of in 2D exponentially increases the computational complexity of the resulting linear system. We propose a patch-wise formulation which enables scalability of the method and allows us to reconstruct 3D velocity within arbitrary regions. On the data acquisition side: 3D vector reconstruction requires at least three Doppler images, each from a different view direction. However, colour Doppler acquisition is restricted by acoustic windows, so available view angles will be limited and will vary greatly between individuals. Colour Doppler images are noisy, and overall image quality depends greatly on anatomy of individuals. In addition the relative transformation between views must be accurately known, which we propose can be achieved using image registration. Each of these factors will influence the accuracy of 3D vector reconstruction. To determine the size of these effects we carry out a detailed sensitivity analysis using simulated data, and compare the results with 3D velocity reconstructed using echo data from three healthy volunteers and three patients.

In summary, the contribution of this paper is threefold: 1) it provides a scalable 3D flow reconstruction method which integrates Doppler information from multiple views, by reformulating the method by Arigovindan et al. (2007) into a 3D patch-wise approach; 2) it identifies and characterises the main parameters which contribute to inaccuracy of 3D velocity reconstruction in a clinical scenario and 3) it provides the range of these parameters for which 3D flow can be accurately reconstructed.

2. Methods

Calculation of 3D velocity vectors from multiple colour Doppler images using a patch-wise, regularized algorithm, is performed in two steps:

1. Registration of B-Mode images (Sec. 2.1).
2. 3D velocity reconstruction of the vector field which best fits the input Doppler data using error minimization, where the error function incorporates physical constraints (Sec. 2.2).

Additionally we propose a simulation framework for assessing the sensitivity of the reconstruction method to different parameters. In particular a simple yet more realistic model for noise and variations in colour Doppler images is proposed (Sec. 2.3).

2.1. Image Registration

In order to combine Doppler information from multiple N_v views the relative position between these views must be known. We calculate these relative positions using a registration algorithm which uses the phase-based similarity measure proposed by Grau et al. (2007), specifically designed for registration of multi-view 3D B-Mode echo images acquired from different acoustic windows. This similarity measure is based on the fact that the Fourier terms of an image are in-phase at edges (Mulet-Parada and Noble, 2000), and therefore high phase congruency across scales indicates presence of edges or features that can be used for registration. As proposed by Grau et al. (2007), registration was initialized by a point wise registration from three manually picked landmarks.

Colour Doppler acquisitions contain a B-Mode image and a colour-coded velocity image. These B-Mode images have a reduced Field of View (FoV) due to the large processing requirements for Doppler acquisition. This reduces the accuracy and capture range of the registration algorithm.

Our solution is to use a two-step registration approach where we also acquire a standard B-Mode image directly after each Doppler acquisition. The two steps of the registration are represented in Fig. 1. Our method firstly registers the reduced FoV B-Mode image to the corresponding standard (wide FoV) B-Mode image, which yields the matrix $M_{L_i}^{r_i}$, where r_i indicates the i-th reduced FoV image and L_i indicates the i-th wide FoV image as shown in Fig. 1 (a). This registration is easy to achieve as the images have been acquired from the same position. Then the wide FoV B-Mode images from N_v different views are registered to one of them, arbitrarily chosen as reference, which yields a set of matrices $M_{L_{ref}}^{L_i}$ $(i = 1 \dots N_v)$ as shown in Fig. 1 (b). Therefore the resultant transformation between two Doppler views can be calculated from $M_{reg} = M_{L_{ref}}^{L_i} \times M_{L_i}^{r_i}$.

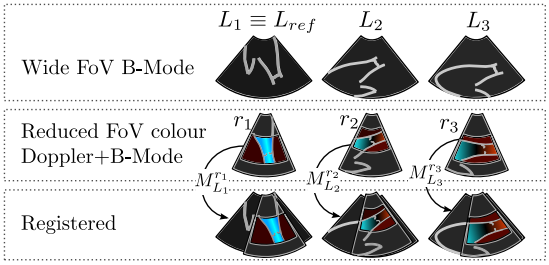

(a) Registration of the standard wide FoV B-Mode images to the B-Mode images from the colour Doppler acquisitions, which yields the matrices $M_{L_i}^{r_i}$.

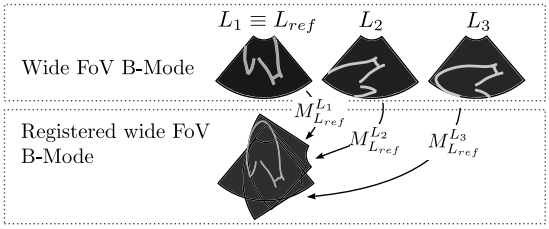

(b) Registration of the standard wide FoV B-Mode images to the reference B-Mode image, which yields the matrices $M_{L_{ref}}^{L_i}$.

Figure 1: Two step registration process. (a) Since the background B-Mode images acquired in a colour Doppler scan have reduced FoV, they are first registered to a standard B-Mode image (wide FoV) acquired from the same view. (b) This is then registered to a reference B-Mode image acquired from a different view. The matrix to transform the colour Doppler images to the reference B-Mode image is $M_{reg_i} = M_{L_{ref}}^{L_i} \times M_{L_i}^{r_i}$.

2.2. 3D Flow reconstruction from Multiple Echo Doppler Views

2.2.1. Description of the general solution

B-splines are smooth functions widely used in signal and image processing for their numerous advantages (Unser, 1999). Our method consists in solving a B-spline based linear system extended from Arigovindan et al. (2007). The full extension to 3D is described in Appendix A. In this section, the method is briefly presented. Let β^n be the B-spline of degree n, we note the scaled and displaced version as $\beta^n(t/s - l) = \beta^n_{s,l}(t)$.

Let $\mathbf{v}(\mathbf{p}) = [v_x(\mathbf{p})\ v_y(\mathbf{p})\ v_z(\mathbf{p})]^\top$ be the fluid velocity field evaluated at the point $\mathbf{p} = [p_x\ p_y\ p_z]^\top$. We can express $\mathbf{v}(\mathbf{p})$ in the space of uniform B-splines of degree n:

$$v_\gamma(\mathbf{p}) = \sum_{i=1}^{N_g^i}\sum_{j=1}^{N_g^j}\sum_{k=1}^{N_g^k} c^\gamma_{i,j,k}\beta^n_{s,i}(p_x)\beta^n_{s,j}(p_y)\beta^n_{s,k}(p_z) \tag{1}$$

where $\gamma \in \{x, y, z\}$, the B-spline grid has a size of $N_g^i \times N_g^j \times N_g^k$ and $\{c^x, c^y, c^z\}_{i,j,k}$ are the B-spline coefficients. The parameter s is the distance between grid nodes and determines the finest resolution of the resulting vector field (i.e. its scale). Each registered view provides an input Doppler data set $\{m_i, \mathbf{p}_i, \hat{\mathbf{d}}_i\}_{i=1\ldots K}$ where for each point i, m_i is the (projected) velocity measurement at position $\mathbf{p}_i$ where the echo beam direction is $\hat{\mathbf{d}}_i$ and K is the total number of input data points. Combining all views, the velocity field $\mathbf{v}$ is the solution that minimises the following energy term

$$J_{proj}(\mathbf{v}) = \sum_k \|\hat{\mathbf{d}}_\mathbf{k} \cdot \mathbf{v}(\mathbf{p}_k) - m_k\|^2 \tag{2}$$

Plugging (1) into (2) the energy can be rewritten in matrix form as

$$J_{proj}(\mathbf{C}) = \|\mathbf{DSC} - \mathbf{m}\|^2 \tag{3}$$

where $\mathbf{C}$ is the B-spline coefficient matrix and $\mathbf{S}$ is the B-spline sampling matrix. Equation (3) may be minimised taking the derivative with respect to $\mathbf{C}$, and equating to zero yields

$$\mathbf{C} = \mathbf{A}^{-1}_{proj}\mathbf{b} \tag{4}$$

where $\mathbf{A}_{proj} = \mathbf{S}^\top\mathbf{D}^\top\mathbf{DS}$ and $\mathbf{b} = \mathbf{S}^\top\mathbf{D}^\top\mathbf{m}$. The reconstructed velocity field at the points sampled by $\mathbf{S}$ can be obtained as $\mathbf{V} = \mathbf{SC}$.

The proposed linear system may not always be well posed, *e.g.* A_{proj} might not be invertible. The system can be regularised by introducing a penalty term proportional to the divergence of the velocity. By penalising the divergence in 3D, we are imposing that the flow should be incompressible, which should yield a more realistic result since blood flow is assumed incompressible.

The divergence can be penalised by adding a function of $\nabla \cdot \mathbf{v}(\mathbf{p}) = 0$ to (2). This strategy is particularly well suited to B-spline grids because the derivative of B-splines can be analytically computed, therefore divergence can be expressed as a function of B-spline coefficients. This allows us to formulate the problem as a linear matrix equation and is thus solvable by LMS as in the non-regularised case. The new energy function is

$$J(\mathbf{v}) \quad = \quad (1-\lambda)J_{proj}(\mathbf{v}) + \lambda J_{div}(\mathbf{v}) \tag{5}$$

where λ is a weighting factor that controls the amount of regularisation and

$$J_{div}(\mathbf{v}) = \sum \|\nabla \cdot \mathbf{v}\|^2$$

All the mathematical development and formulation in matrix form can be found in Appendix A.

2.2.2. Computational Complexity, Scalability and Patch-Wise Formulation

3D velocity reconstruction, as described in Sec. 2.2.1 is a matrix-based linear problem. Matrix size depends on the number of input data points and the size of the B-spline grid. These two quantities increase with the number of input views, with the extension to the third dimension and with the use of fine grids, resulting in severe memory limitations and lacking of scalability. One way of reducing the computational requirements is to divide the B-spline grid into patches where 3D velocity is computed independently, as shown in 2D (for ease of illustration) in Fig. 2. Because B-splines have a finite support, we compute the coefficients in a patch by taking input

data within a subset of the input domain. The computation patch P is moved across the B-Spline grid to cover all the nodes.

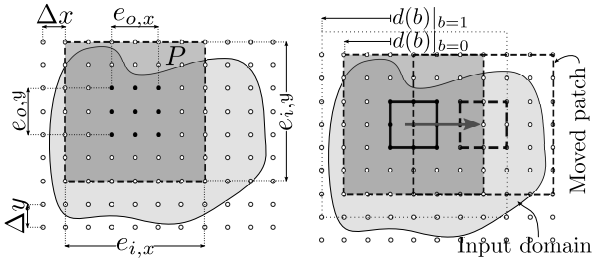

(a) Patch definition. (b) Patch overlap.

Figure 2: 2D representation of the patch-wise division of the reconstruction grid, for B-splines of degree $n = 3$. (a) The patch size is defined by the input extent (e_i, region of input data used to calculate the coefficients of this patch) and output extent (e_o, region covering the coefficients that are calculated in this patch). (b) Example of e_i for values of the border $b = 0$ and $b = 1$. The dashed patch on the right represents where the patch is moved next to compute next set of coefficients.

The patch P is defined by two extents, the output extent e_o and the input extent e_i, described in Fig. 2 (a). The exact solution is obtained only if a single patch covers the whole input domain, which is the method used by Arigovindan et al. (2007). If e_i covers only a subregion of the input domain the solution is approximated but the memory usage is reduced. The approximation improves as more input points are used. Since a B-spline of degree n extinguish at $(n + 1)/2$ grid points from the B-spline centre, we propose that for calculating each coefficient, all the points within a minimum distance $d_{min} = (n+1)/2 \times [\Delta x\ \Delta y\ \Delta z]^\top$ shall be taken into account, as represented in Fig. 2 (b). To improve accuracy, d_{min} can be extended by an amount b (border parameter) selected by the user. This way, we include in the calculation of each coefficient all the input data within a distance $d(b) = [(n+1)/2+b]\times[\Delta x\ \Delta y\ \Delta z]^\top$.

To reconstruct the velocity field across the whole region of interest, the patch is moved in such a manner that the external points of two consecutive patches overlap (Fig. 2 (b)). The overlap is therefore of $[(n + 1)/2 + b]$ nodes. Because of the overlap, the coefficients at the overlapping region are computed several times; however, all the coefficients outside e_o are discarded.

2.3. Simulations

The aim of the simulations was to asses the effect of different factors on the accuracy of 3D velocity reconstruction, and from there establish the range of values which enable accurate 3D velocity reconstruction. The ability to freely vary view directions, amounts of image noise, and to calculate image registration accuracy are all extremely difficult to achieve using real echo images. View directions are restricted by acoustic access and image quality varies greatly between individuals. All these factors can however be directly controlled using simulated colour Doppler images.

2.3.1. Simulation of colour Doppler images from from 3D+t Flow MRI

Simulated colour Doppler images were generated from 3D+t Flow MRI acquired in a healthy volunteer, as shown in Fig. 3:

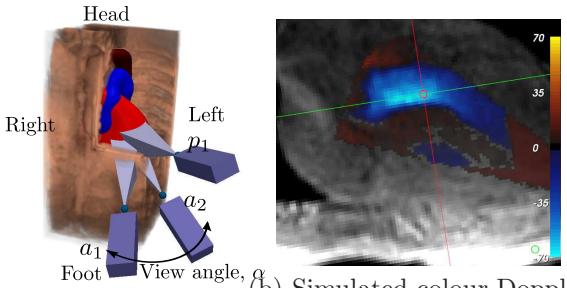

(a) Virtual probe locations (b) Simulated colour Doppler from a_1

Figure 3: Virtual probe locations in the PC-MRI dataset from which simulated colour Doppler images are generated. (a) a_1 and a_2 show transducer position located at an apical window, separated by a view angle $\alpha = 25°$, and p_1 shows transducer position located at a parasternal window. In all cases the virtual probe is oriented towards the aortic valve. As an example, (b) shows a zoomed 2D slice through the resulting 3D colour Doppler image, during systole, for probe position a_1.

Three virtual probe locations were manually selected from clinically-feasible locations with respect to the anatomy in the MR images. From these locations, frustum shaped volumes were generated pointing towards the aortic valve (Fig. 3 (a)). Colour

Doppler images were simulated by projecting the 3D+t Flow MRI velocity vectors onto the direction defined by the frustum vertex and each data point (Fig 3 (b)). The resulting views, plus the knowledge of their relative positions, were used by our algorithm to produce a reconstructed 3D flow field.

2.3.2. Novel Noise Model for Colour Doppler Images

Previous work (Xu et al., 1991; Maniatis et al., 1994; Arigovindan et al., 2007) assumes that noise in Doppler images is voxel-wise additive Gaussian noise. However, observations of noise and variations in real Cartesian colour Doppler images do not seem to follow this model, but seem to occur at a larger scale. These variations can be appreciated in the first row of Fig. 6, and compared to voxel-wise additive Gaussian noise shown in the third row of the same figure. Therefore we propose a new multi-scale model:

$$I = D + G(\sigma_f) + L_s(\sigma_L) \tag{6}$$

where D is the noiseless image where voxel intensity represents the value of the underlying velocity projected along the echo beam direction, G and L_s are voxel scale and large scale noise components, respectively, both centred and with standard deviations σ_f and σ_L, and I is the noise-perturbed realistic image. If I is regarded as a discrete sampling of a continuous $3D$ signal Υ over a discrete grid with spacing $(\Delta x, \Delta y, \Delta z)$, the terms of (6) are mathematically defined by

$$D = \Upsilon \times \sum_i \sum_j \sum_k \delta(\frac{x}{\Delta x} - i)\delta(\frac{y}{\Delta y} - j)\delta(\frac{z}{\Delta z} - k) \tag{7}$$

$$G(\sigma_f) = \sum_i \sum_j \sum_k g_{i,j,k}(\sigma_f)\delta(\frac{x}{\Delta x} - i)\delta(\frac{y}{\Delta y} - j)\delta(\frac{z}{\Delta z} - k) \tag{8}$$

$$L_s(\sigma_L) = \sum_u \sum_v \sum_w g_{u,v,w}(\sigma_L)\delta(\frac{x}{s\Delta x} - u)\delta(\frac{y}{s\Delta y} - v)\delta(\frac{z}{s\Delta z} - w) \tag{9}$$

where $g_{i,j,k}(\sigma_f)$ and $g_{i,j,k}(\sigma_L)$ are random values following a centred Gaussian distribution with variances σ_f^2 and σ_L^2 respectively. To perform the sum in (6) we resampled $L_s(\sigma_L)$ to the grid defined by D by using cubic B-spline interpolation.

The Gaussian voxel-wise model is often justified because the received Doppler signal is related to the concentration of scatterers in blood (i.e. red cells), which is also believed to have a Gaussian distribution (Angelsen, 2000; Pastorelli et al., 2008). However, many non Gaussian effects contribute to noise in the final colour Doppler image, from acquisition phenomena such as Rayleigh fading, intrinsic spectral broadening of Doppler signal and non-uniformity of the ultrasound beam (Gill, 1985; Hoskins et al., 2010) to preprocessing of the data such as filtering and scan-conversion. In addition, uncontrolled external changes, like physiological changes, involuntary changes in probe location, pressure of the probe against the skin and small changes in velocity scale (Fan et al., 1994) also contribute to changes in Doppler images. All these combined effects can produce important intra-machine and inter-machine variability of colour Doppler images, as discussed by Fan et al. (1994).

The goal of our noise model is not to represent the underlying physics of colour Doppler image formation, but to produce realistic perturbations on Cartesian converted colour Doppler images in a simple way. Therefore (6) models all the acquisition and preprocessing chain, which includes Cartesian conversion, filtering and smoothing for display.

Our proposed noise model needs three input parameters: the scale s for the large scale noise component L_s, the variance of the voxel-scale noise component σ_f^2 and the variance of the large scale noise component σ_L^2. In the following sections we firstly describe how we estimate the value of s, and then obtain a value for the ratio between the amounts of large (σ_L^2) and small (σ_f^2) scale noise, so we can compare our proposed model with a standard voxel-scale noise model.

Finding the appropriate scale for the noise model. To obtain the scale for the proposed noise model, we acquired several consecutive colour Doppler images without moving the probe and compared them using the Sum of Squared Differences (SSD) measure, at different values of the scale s. The representation I^s

of an image I at a scale s is defined as the best approximation, in a Least Mean Squares (LMS) sense, of I in a B-spline grid where node spacing is determined by s:

$$\begin{aligned} I^s(\mathbf{p}, \mathbf{C^s}) &= \sum_i \sum_j \sum_k c^s_{i,j,k} \beta^n_{s,i}(p_x) \beta^n_{s,j}(p_y) \beta^n_{s,k}(p_z) \iff \\ \mathbf{I^s} &= \mathbf{S}(s)\mathbf{C^s} \end{aligned} \tag{10}$$

where $\mathbf{I}$ and $\mathbf{I^s}$ are column vectors with all the voxel values of I and I^s, $\mathbf{S}$(s) is the B-spline sampling matrix at the scale s, defined in (A.5), and the coefficients $\mathbf{C^s} = [\dots c^s_{i,j,k} \dots]^\top$ are calculated by minimising the dissimilarity between I^s and I, in a least mean squares sense analogous to (2):

$$\begin{aligned} & \min_{\mathbf{C^s}} \sum \|I^s(\mathbf{p}, \mathbf{C^s}) - I(\mathbf{p})\|^2 \\ \Rightarrow \quad & \mathbf{C^s} = (\mathbf{S}(s)^\top \mathbf{S}(s))^{-1} \mathbf{S}(s)^\top \mathbf{I} \\ \Rightarrow \quad & \mathbf{I^s} = \mathbf{S}(s)(\mathbf{S}(s)^\top \mathbf{S}(s))^{-1} \mathbf{S}(s)^\top \mathbf{I} \end{aligned} \tag{11}$$

To estimate the size of the large scale noise, the mean sum of square differences $mSSD(s)$ between the n images at scale s is calculated:

$$mSSD(s) = \frac{2}{n(n-1)} \sum_{i=2}^{n} \sum_{j=1}^{i-1} \overline{\|I^s_i - I^s_j\|^2} \tag{12}$$

where $\overline{\|\cdot - \cdot\|^2}$ indicates the average SSD between two images.

Figure 4 illustrates how the large scale is chosen. Figure 4 (a) represents a slice of I^1 and I^2 at different scales. These comparison between both images is shown in Fig. 4 (b), which shows values of $mSSD(s)$ over a range of scales. At large scales (right hand side of Fig. 4) the images will be very blurred and $mSSD(s)$ will represent the squared difference between the mean values of the images. As the scale is reduced, features in the individual images become more distinct, and there is a scale at which features between the different Doppler images match (s_M). As the scale is further decreased we observe large scale variations between the images which initally increase $mSSD(s)$ slightly, but $mSSD(s)$ remains constant over a range of values of s. This region is denoted by the dashed ellipse in Fig. 4, and it is over these range of values that we propose our large scale noise should be calculated. As s is further reduced $mSSD(s)$ increases which is caused by small scale, (voxel-wise when $s = 1$) differences between the images. Therefore, we propose using $s = 15$ for the size of our large scale noise, which is approximately in the middle of the range for the datasets we have tested.

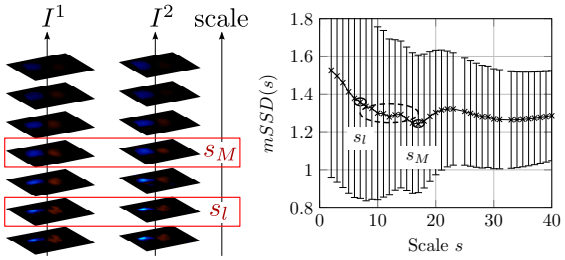

(a) Two images at different scales.

(b) mSSD between images.

Figure 4: Finding the scale at which variations occur. (a) Slices of two images represented at different scales. (b) Mean value and standard deviation of the mSSD, between images from one view (averaged over all frames), with respect to the scale s. The x axis represents the scale. The curve minimum, indicates the scale s_M for which the large scale features of both images best match. A dashed ellipse indicates the range of scales where the large scale variations occur.

Finding the ratio between amount of large-scale σ_L and voxel-scale noise σ_f. The ratio between σ_L and σ_f was chosen so that the proposed multi scale noise model and the standard voxel-wise noise model (of variance σ_{vw}) could be compared. We propose that the level of noise represented in both models is similar if the reconstructed velocity vectors have similar average angle and magnitude error. Figure 5 shows the average error in angle and in magnitude for a voxel-wise noise model compared to a large scale noise model, when $\sigma_{vw} = \sigma_L$ for different values of σ_f. It can be shown that the curves agree well for $\sigma_f = \sigma_L/2$, thus this was the value chosen for our model.

The proposed multi-scale noise model produces more visually realistic variations in colour Doppler images than the standard Gaussian voxel-wise model. Figure 6 show an example of three real colour Doppler images acquired from the same view (a)–(c), and similar images simulated with our proposed method (d)–(e) and with the standard voxel-wise approach (f)–

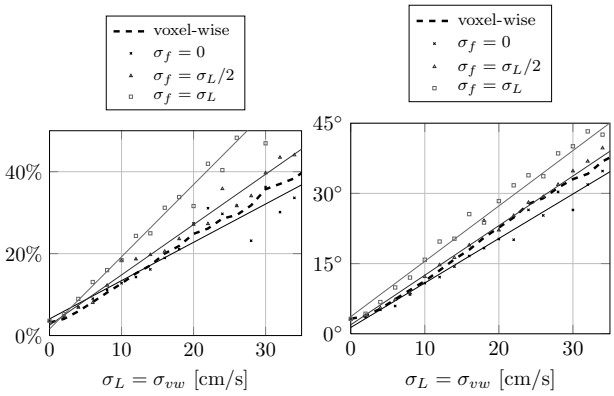

(a) Error in magnitude (b) Error in angle

Figure 5: Noise dependence in velocity magnitude in simulated data, for different values of the ratio between large scale and voxel scale noises, σ_f/σ_L.

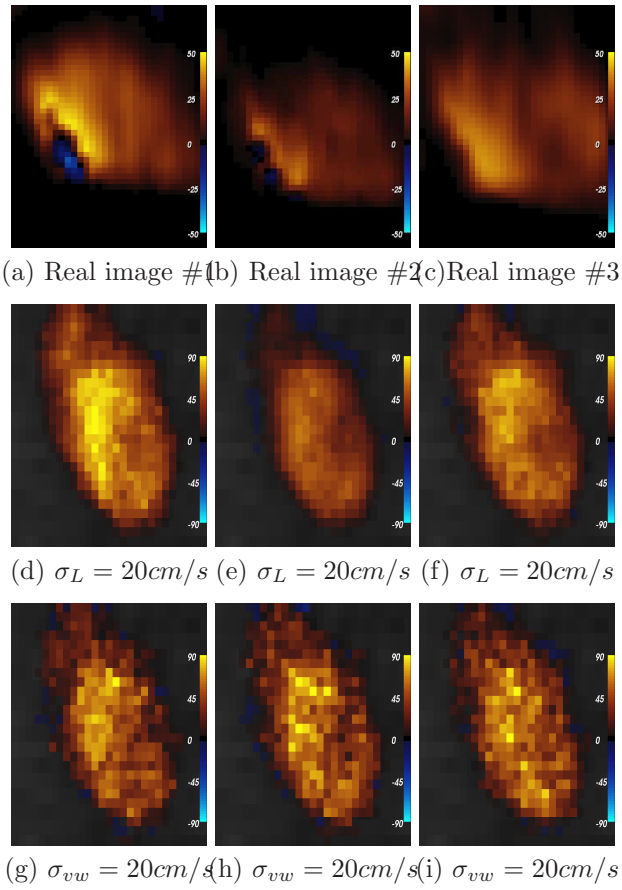

(a) Real image #1 (b) Real image #2 (c) Real image #3

(d) $\sigma_L = 20cm/s$ (e) $\sigma_L = 20cm/s$ (f) $\sigma_L = 20cm/s$

(g) $\sigma_{vw} = 20cm/s$ (h) $\sigma_{vw} = 20cm/s$ (i) $\sigma_{vw} = 20cm/s$

Figure 6: Comparison of real and simulated colour Doppler images. (a)–(c) Slice of three real colour Doppler images acquired consecutively from the same view, showing variations that occur in colour Doppler images. (d)–(f) Three simulated colour Doppler images, produced from 3D+t Flow MRI, acquired from a virtual view manually chosen to be close to the view position of (a), and approximately the same cardiac phase. The three images have been generated from exactly the same view and for each of them our proposed multi-scale noise has been used ($\sigma_L = 20cm/s$, $\sigma_f = \sigma_L/2$). (g)–(i) Simulated images produced in a similar way as (d)–(f) but with added voxel-wise noise ($\sigma_{vw} = 20cm/s$). Our multi-scale noise model produces more realistic variations than the typical voxel-wise Gaussian model.

(g). From visual inspection it can be appreciated that our proposed method models variation in colour Doppler images which are much more realistic when compared to real Doppler acquisitions than the voxel-wise approach.

3. Materials and Experiments

In this section we describe the experiments carried out on simulated data and real data. Experiments on simulated data were designed to estimate view angles, noise level of input data and registration accuracy required to enable accurate 3D blood velocity reconstruction. The outcome of the simulation study was verified with real data from three healthy volunteers. We also carried out a preliminary test on patient data from three paediatric patients to show feasibility and compliance with current clinical protocols.

3.1. Experiments on Simulated Data

We carried out experiments to evaluate the sensitivity of flow reconstruction to two different kinds of parameters:

- Algorithmic parameters: we considered the error introduced by the method itself, which is produced by the combined effect of B-spline fitting of input data, regularisation and patch-wise computation.
- External factors: we investigate three parame-

ters that could have a major impact on reconstruction accuracy:

- Noise in colour Doppler images.
- Registration accuracy.
- Range of view angle.

The reconstructed velocity fields obtained were compared to the ground truth in the following way, which allowed us to extrapolate results to real data. We carried out measurements of three errors: mean error in velocity magnitude, mean error in velocity angle, and mean error in flow rate through the ascending aorta, using exactly the same surface and the same segmentation in the simulated data as in the ground truth. Although error in flow rate represents an indirect measurement of accuracy through a scalar, it was chosen because it can also be compared to real volunteer data, for which a ground truth velocity field was not available, but flow rate could be calculated from 2D+t Flow MRI.

3.1.1. Sensitivity to Algorithmic Parameters

We report experiments on the dependence of accuracy with the value of the border width (b). We also measured the effect of regularisation (5) on the reconstruction accuracy, for different values of λ.

3.1.2. Sensitivity to External Factors

In subsequent experiments, noise in input data in the range $0cm/s \leq \sigma_L < 40cm/s$ are used which are consistent with Doppler noise levels described in the literature (Arigovindan et al., 2007; Pastorelli et al., 2008) and cover the range of values experienced in our volunteer experiments (Sec. 4.2 and Fig 6).

Noise in colour Doppler data. We assess the reconstruction accuracy for different amounts of multiscale noise (6). As described in Sec. 2.3.2, our noise model has three parameters: scale at which large variations occur, which is fixed to $s = 15$; standard deviation of the large scale component of the noise model, σ_L; and standard deviation of fine scale component of the noise model, σ_f, which is fixed to $\sigma_f = \sigma_L/2$.

Registration accuracy. We simulate registration errors by adding Gaussian noise to the rigid registration parameters of one of the three views. The phase-based similarity measure that we used to register the three views (Grau et al., 2007), reports Target Registration Error (TRE) as described by Fitzpatrick (2001) below $2mm$ in more than 70% of the cases, the rest of which are in the range $[2mm, 5mm]$. Therefore, we model registration error by perturbing the rigid parameters of the registration matrix in order to obtain values of the TRE in the interval $[0mm, 5mm]$. This was achieved as follows: 100 random rigid transformation matrices were produced and used to transform one of the three views. For each matrix, the TRE was calculated as the average displacement, in mm, of 100 landmarks randomly placed within a 15mm radius from the centre of the Left Ventricular Outflow Tract (LVOT) segmentation used for flow rate computation. The transformed images were used to reconstruct velocity vectors.

View angle. At least three colour Doppler views are required to reconstruct 3D velocity. We believe that the angle between views has an important impact on reconstruction accuracy. In clinical practice, view angles are limited by anatomy and acoustic windows. We found a clinically feasible protocol to obtain three relatively independent views using a combination of two apical views and one parasternal view as represented in Fig. 3 (a). The angle between the apical views and the parasternal is usually fixed by anatomy. The echocardiographer can more easily move the probe within the four-chamber plane to separate the two apical views by an angle α. For this reason we study the influence of α on reconstruction accuracy.

We simulated the acquisition of colour Doppler images from sets of three views, as shown in Fig. 3 (a). The parasternal view and one apical view (beam sources at p_1 and a_1 respectively) were kept fixed while the second apical view (beam source at a_2) was placed at the apical window separated from a_1 by an angle α which was varied from 0° to 60° at intervals of 1°.

3.2. Experiments on Real Data From Volunteers

3D Colour Doppler data was acquired targeting the blood flow through the LVOT. Echo exams were acquired using a Philips iE33 system, equipped with a X3-1 transducer for cardiac applications. Image acquisitions consisted of 3D+t sequences acquired from 3 different views. At each view, an expert echocardiographer acquired three consecutive sequences without moving the transducer, to measure noise between similar acquisitions. Under ideal conditions these three sequences would be identical, however images vary due to involuntary changes in anatomy or in probe location and noise and variability in colour Doppler images. Access to reformatted Cartesian echo images was via the Philips Healthcare QLab software, using either 2D+t screenshots (colour Doppler) or via a dedicated software patch (B-Mode images).

Any sequences which failed registration or where the image quality was clearly poor were discarded. This was done by visual inspection. In our three volunteers, 7.5% of the input images were discarded. When for the same view colour Doppler images differed significantly, we assumed that the colour Doppler image with more signal was more accurate. Only this image was then used as input for the velocity reconstruction process described in Sec. 2.

Care was taken when selecting the Doppler velocity range to avoid aliasing. However some aliasing still occurred. For these images, aliasing was unfolded using a semi-automatic method described in Appendix B.

The reconstructed velocity fields were evaluated qualitatively and quantitatively. Qualitative analysis was carried out by clinicians who scored the image quality and plausibility of the resulting flow patterns and velocity profiles (bad – average – good).

Quantitative accuracy measurements were carried out comparing flow rate curves obtained from our proposed method to flow rate obtained from standard temporally resolved through-plane flow-encoded 2D MRI (2D+t Flow MRI), calculated at the ascending aorta. Flow curves were integrated through time to compute stroke volume, which was also compared between the two modalities. 2D+t Flow MRI was acquired on a 3 Tesla MR System (Achieva Philips, Best, The Netherlands) including a clinically used phase contrast sequence with the following parameters: k-space segmented acquisition retrospectively triggered with the subjects electrocardiogram (ECG), spatial resolution: $2.5 \times 2.1mm^2$, slice thickness: $8mm$, temporal resolution: $25ms$, velocity encoding range: $150cm/s$. Data was acquired during a breath-hold of approximately $18s$. Care was taken to align the acquired slice perpendicularly to the main flow direction.

3.3. Experiments on Patient Data

We report results on three paediatric congenital patients, and compare them to 2D+t Flow MRI acquired immediately before the echo. Patient 1 was 2 years old with Hypoplastic Left Heart Syndrome (HLHS) post Hemifontan procedure. Five colour Doppler views were acquired with a Philips X3-1 probe during breath-holds, targeting the tricuspid valve: 2 apical, 1 parasternal, 1 subcostal and 1 parasternal oblique. A standard B-Mode sequence was acquired in each view for image registration. Patient 2 was 3 months old with HLHS post stage 1 procedure. Three colour Doppler views were acquired with a Philips X7-2 probe during breath-holds, targeting the tricuspid valve: 1 apical, 1 parasternal and 1 subcostal. Patient 3 was 2 months old with repaired critical aortic stenosis. Three colour Doppler views were acquired with a Philips X7-2 probe during breath-holds, targeting the left ventricular chamber: 1 apical, 1 parasternal and 1 subcostal. At each view, the probe was tilted along three orientations in order to achieve maximum ventricular coverage (therefore 9 images were acquired).

In all cases, two consecutive sequences were acquired in each view, with a time delay between each acquisition of $40ms$. These sequences were interleaved to increase temporal resolution. The echo acquisition protocol for each patient took less than 10 minutes to complete. The interleaved sequence had a temporal resolution of between 24 and 30 frames per cardiac cycle. All three patients were under general anaesthesia with active respiratory control. Images were acquired with institutional ethical approval after informed parental consent.

4. Results

4.1. Results on Simulated Data

4.1.1. Inaccuracies Intrinsically Introduced by the Proposed Method

Figure 7 (a) shows the dependency of error in flow rate with the patch border size b. Larger values of b rapidly yield values of the patch coefficients very close to the true solution. Since the computation time increases exponentially with b, we use $b = 3$ for B-spline degree (d_{bs})= 1, and $b = 5$ for d_{bs}= 3 which assure less than 2% error. The size of the patches did not have any effect on flow rate accuracy for values of b greater than 1.

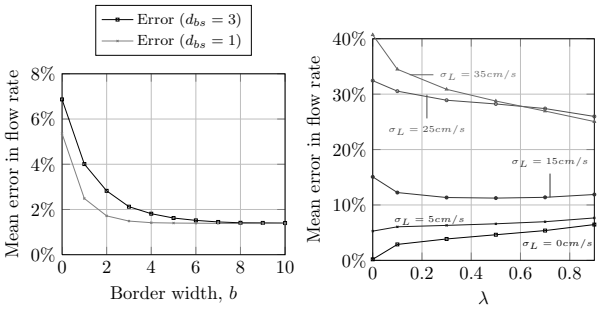

(a) Error in flow rate for different values of b

(b) Error in flow rate for different values of λ

Figure 7: Relative reconstruction error in simulated data, with respect to the ground truth, for different values of algorithmic parametres.

Figure 7 (b) shows the effect of regularisation on accuracy of reconstructed velocity fields for different amounts of noise. The amount of regularisation is driven by the value of λ, as described in (5). In absence of noise, regularization introduces some error (see curve for $\sigma_L = 0cm/s$) because it smoothes the resulting vector field. For noisy data ($\sigma_L > 5cm/s$), just a small amount of regularisation ($\lambda \geq 0.1$) improves results.

4.1.2. Contribution of Noise in Colour Doppler Data

Figure 8 shows the evolution of the mean error in flow rate, as a percentage of the maximum flow rate of the ground truth, with respect to the amount of noise, both for our proposed noise model (6) and the voxel-wise noise model. Although both errors increase linearly with the amount of noise, with our proposed large scale noise model mean error increases much more rapidly. Therefore, a standard additive voxel-wise noise model could greatly overestimate algorithm accuracy.

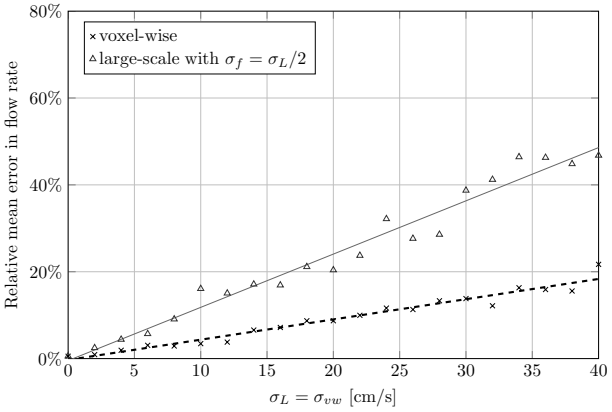

Figure 8: Error in the calculation of flow rate from simulated data, with respect to the amount of noise, for two noise models: our proposed large scale noise (6) for which the horizontal axis represents σ_L, and $\sigma_f = \sigma_L/2$; and voxel wise noise of standard deviation $\sigma_{vw} = \sigma_L$ added to simulated colour Doppler images.

Our algorithm is much less sensitive to voxel-wise Gaussian noise than it is to our noise model for two reasons: 1) Flow rate is computed by integration, which acts as a low pass filter removing spatial-high frequency noise inherent to voxel-wise scale, and 2) the LMS minimization is optimal for Gaussian noise.

4.1.3. Contribution of Registration error

Figure 9 shows the influence of registration accuracy on the accuracy of the reconstructed velocity, for $\sigma_L = 20cm/s$ and $\sigma_f = \sigma_L/2$. The plots of flow rate, angle and magnitude errors are all almost flat for registration errors between 0 and $2.5mm$, indicating that registration errors $< 2.5mm$ have very little effect on vector reconstruction accuracy which is dominated by the $\sigma_L = 20cm/s$ noise used in this simulation.

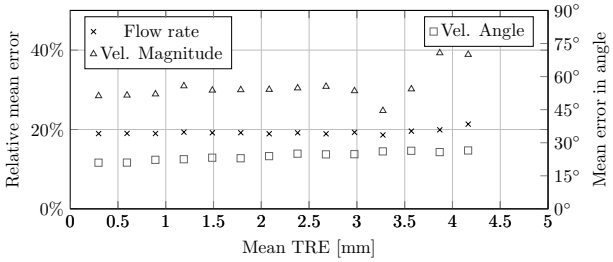

Figure 9: Effect of Target Registration Error (TRE) on accuracy of flow rate and velocity magnitude (left y-axis) and velocity angle (right y-axis), for $\sigma_L = 20cm/s$, and $\sigma_f = \sigma_L/2$.

4.1.4. Contribution of View Angle

Figure 10 shows the impact of the view angle on the reconstruction accuracy, for simulated data with added noise with $\sigma_L = 20cm/s$, and $\sigma_f = \sigma_L/2$. Small angles ($\alpha < 20°$) make the reconstruction error increase steeply. Larger angles keep the mean error almost flat. From this we conclude that if the view angles are above 20°, the reconstruction error is mostly determined by the noise in colour Doppler data.

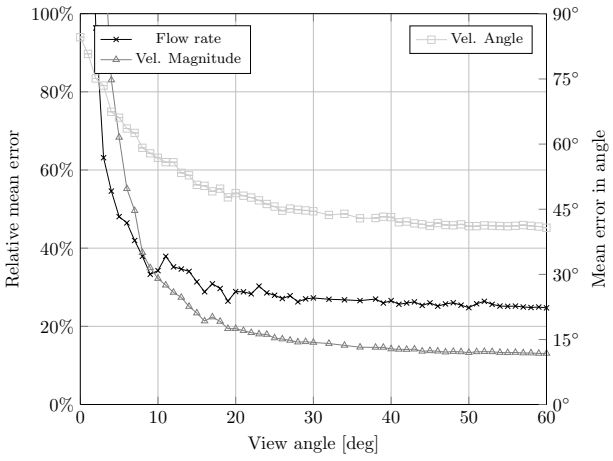

Figure 10: Effect of view angle on reconstruction accuracy of flow rate and velocity magnitude (left y-axis) and velocity angle (right y-axis), for a noisy case with $\sigma_L = 20$ and $\sigma_f = \sigma_L/2$.

Summary. Table 1 shows a summary of the impact and ranges of different parameters on reconstruction accuracy. Typical values for noise and view angle were calculated from our experiments on adult volunteer data (Fig. 11), and the values for registration accuracy are those reported by Grau et al. (2007).

	Impact	Required Range	Typical Range
Noise	Large	$< 10cm/s$	5% – 60%
TRE	Small	$< 2.5mm$	$< 2mm$
View Angle	Large	$> 20°$	10°–40°

Table 1: Summary of contributors to inaccuracy of 3D velocity reconstruction: noise of input data, Target Registration Error (TRE) and view angles. The required range of noise ($< 10cm/s$), obtained from simulations, corresponds to a 7% of the maximum velocity.

4.2. Results on Volunteer Data

We report results on three healthy volunteers, who varied greatly in terms of their image quality and acoustic access. This variation enabled us to validate the results of the simulation studies presented in Sec. 4.1, by producing simulated data with noise and view angles measured from the three volunteers. The flow predicted from these simulations was compared to the results obtained from volunteer data.

4.2.1. Quantitative Assessment of Reconstruction Accuracy

Figure 11 (a) shows measurements of angles and image quality and Fig. 11 (b) shows measurements of noise of the input data for each volunteer. Noise measurements were calculated for both models: voxel-wise noise and multi-scale noise ($s = 15$). As expected, data which visually showed good or average image quality (volunteers 1 and 3) had lower amount of noise than data which showed bad image quality (volunteer 2). Only one (volunteer 1) of three volunteers had all three view angles above 20°. It was therefore expected that reconstruction for volunteer 2 would be inaccurate due mainly to high noise, and that reconstruction for volunteer 3 would be inaccurate due to small view angles ($< 15°$).

	Volunteer		
	1	2	3
$\alpha[deg]$	44	17	39
$(p_1\hat{,}a_1)$	37	31	15
$(p_1\hat{,}a_2)$	22	39	29
Q	avg.	bad	good

(a)

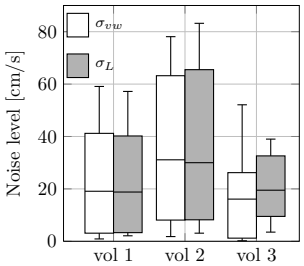

(b)

Figure 11: Measurements on volunteer data. (a) View angles: angle between apical views (α), and angle between the parasternal view and each of the apical views ($(p_1\hat{,}a_i)$). Angles lower than 20° are expected to cause large errors (Fig. 10). Image quality (Q) was assessed by a clinician, blinded to results, based on the quality of B-Mode images. (b) Box and whisker plots of noise level (box shows median and interquartile range, whiskers show 10% and 90% percentiles) from volunteers, measured first voxel-wise (σ_{vw}) and then at a scale $s = 15$ (σ_L).

Table 2 shows the error in stroke volume measured in real data compared to the expected error calculated from simulations with the standard voxel-wise noise model and with our multi-scale noise model. The first column (Real) shows the disagreement between volume calculated from 2D+t Flow MRI and from our proposed technique in the three volunteers. To verify how realistic our simulation study was, we simulated 3D colour Doppler data with the view angles and noise (both voxel-wise and multi-scale noise models) measured for the three volunteers and shown in Fig. 11. Results suggest that voxel-wise noise overestimates the accuracy of the algorithm while our proposed noise model shows good agreement with real data.

As predicted by our noise model, accurate reconstructed flow was achieved for volunteer 1 and large errors were observed for volunteers 2 and 3, compared to 2D+t Flow MRI.

	Real	Simulation	
		voxel-wise	Proposed
Volunt. 1	15.0%	$1.4\% \pm 3.7\%$	$10.8\% \pm 9.6\%$
Volunt. 2	61.9%	$37.9\% \pm 27.3\%$	$61.2\% \pm 59.6\%$
Volunt. 3	74.5%	$1.6\% \pm 2.4\%$	$63.6\% \pm 31.2\%$

Table 2: Error in stroke volume on three healthy volunteers with respect to 2D+t Flow MRI (*Real*), and error on 3 simulated datasets with similar parameters to the real cases. Simulations have been performed using two approaches: the voxel-wise Gaussian noise (*voxel-wise*) and our multi-scale noise model (*Proposed*).

4.2.2. Qualitative Assessment of Reconstruction Accuracy

In addition to the numeric results, we analyse the qualitative information that can be obtained from 3D velocity fields. Figure 12 (a) shows an example of the reconstructed velocity field through the aortic valve, for volunteer 1, in mid systole. The anatomy is represented by three orthogonal slices of a 3D B-Mode image acquired from an apical view. To facilitate interpretation of this image, Fig. 12 (b) shows the projection of the reconstructed velocity field onto a long axis plane of the left ventricle centred in the LVOT.

Qualitative analysis of the 3D flow patterns throughout the cardiac cycle was carried out by a clinician, who considered them all visually plausible. Velocity vectors are colour coded by velocity magnitude. Velocity increases when blood goes through the valve narrowing, and the maximum velocity is not observed along the midline but nearer to the outside of the aortic arch.

Figure 13 shows through plane velocity profiles for volunteer 1 corresponding to the phases of the cardiac cycle indicated by the ECG traces, together with a slice of the B-Mode image on the sampling plane for anatomical reference. The resulting through plane velocity profile follows the expected paraboloid shape skewed towards the aortic wall as has been found in

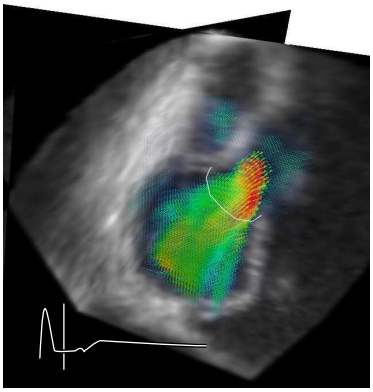

(a)

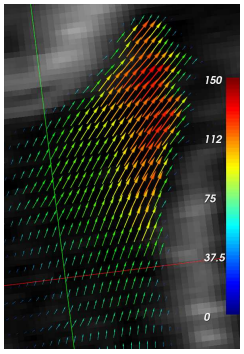

(b)

Figure 12: 3D velocity field reconstruction for volunteer 1. Velocity magnitude is colour coded. This frame corresponds to the middle of left ventricular systole, where blood is ejected from the ventricle through the aorta. (a) 3D rendering of the velocity field with and three orthogonal cuts of a registered B-Mode image for anatomical reference. A white ring represents the plane through which flow was computed. (b) In plane projection of the 3D reconstructed velocity field. Note how velocity magnitude increases in the centre of the outflow tract.

the past by Paulsen and Hasenkam (1983). Since the echo acquisition is ECG-triggered, the first frame (a) corresponds to the instant directly after the R wave (isovolumetric contraction of the left ventricle). Next, the aortic valve opens (b)–(c) with a rapid increase in velocity first and a less steep deceleration later (which explains the lower profile in (c)). The animated sequence over the whole cardiac cycle is included as additional material (Movie 1).

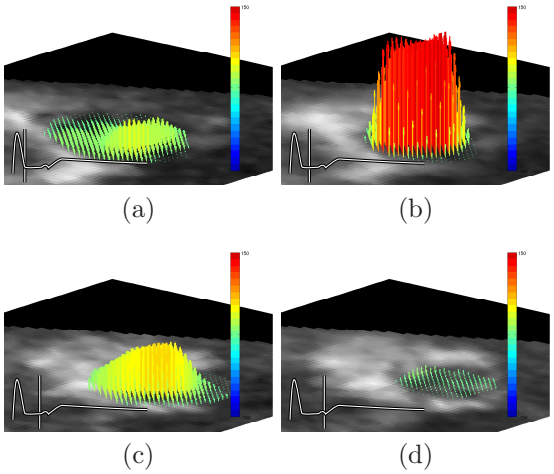

(a) (b) (c) (d)

Figure 13: Through plane velocity profiles at the aortic valve, measured with our method, for volunteer 1. (a) to (d) represent different instants of the ventricular systole, which can be temporally located within the cardiac cycle with the ECG trace. Velocity vectors are colour-coded by through plane velocity magnitude. Movie 1, showing the velocity profile throughout the full cardiac cycle, is provided as additional material.

4.3. Results on Patient Data

Quantitative results from the three patients were obtained by comparing flow volume to 2D+t Flow MRI. For patients 1 and 2, representations of the 3D flow are provided for visual inspection and qualitative analysis of the reconstructed velocity fields. For the patient 3, 3D+t Flow MRI was also available and intra-cardiac flow could be visualised with both modalities.

4.3.1. Quantitative Assessment of Reconstruction Accuracy

Table 3 shows the angles measured between each pair of views (each cell shows patient 1 / patient 2 / patient 3). All the angles were equal or larger than 20° except for the angle between the oblique view and the the first apical view (18°) from patient 1, for which four more views with sufficient angles were available. Best view angles were obtained with the subcostal view which, unfortunately, was difficult to obtain in adults.

	A2	P	SC	Ob
A1	28°/- /-	77°/- /54°	30°/73°/24°	18°/20°/-
A2		58°/-/-	53°/-/-	27°/-/-
P			80°/-/70°	84°/-/-
SC				46°/69°/-

Table 3: View angles measured from three patients (pat. 1/pat. 2/pat. 3). Views stand for: A≡Apical; P≡Parasternal; SC≡Subcostal; Ob≡Oblique. Angles below 20° have been highlighted in grey.

The noise could not be quantified in the same way as for the volunteers, since constraints in the duration of the acquisition, fixed by the approved ethics, prevented us from acquiring additional colour Doppler images for noise calculation. Therefore, noise was estimated by assuming that there was no systolic flow through the tricuspid valve during systole and that any nonzero value was due to noise. The median noise level (and inter-quartile range) was $2.0cm/s$ ($3.5cm/s$) for patient 1, $1.8cm/s$ ($8.5cm/s$) for patient 2 and $2.6cm/s$ ($8.7cm/s$) for patient 3. Figure 14 shows an example of the transtricuspid flow rate curve from patient 1, calculated with our method and compared to 2D+t Flow MRI. As predicted given these angles and noise level, and according to the results obtained in our simulation studies, the two curves agreed well with a difference in stroke volume of 13.51%. The absolute stroke volumes and the difference found with respect to 2D+t Flow MRI for patients 2 and 3 yielded similar results and are shown in table 4.

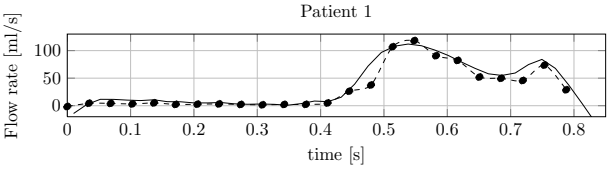

Figure 14: Flow rate on patient 1 through the tricuspid valve. Plane through which flow rate was computed was set at acquisition time for 2D+t Flow MRI, and a similar plane was manually selected in postprocessing for our proposed method.

	Vol. Echo	Vol. MRI	Deviation
Patient 1	24.2	28.0	13.51%
Patient 2	9.9	11.6	14.8%
Patient 3	12.7	14.5	12.6%

Table 4: Stroke volume (inflow) in patient data, in ml, and deviation with respect to the values measured with 2D+t Flow MRI.

4.3.2. Qualitative Assessment of Reconstruction Accuracy

Reconstructed velocity fields were produced from each patient dataset for visual inspection. Figure 15 shows a few selected diastolic frames from patient 1, where blood motion is illustrated by following the motion of particles initially placed in the right atrium. To relate to anatomy, particles are shown on a compounded B-Mode image (Yao et al., 2011). A movie of the entire cardiac cycle has been included as additional material (Movie 2).

The reconstructed velocity field from patient 2 is represented in Fig. 16. In this case, the small size of the patient (3.6kg) enabled the use of a X7-2t probe which has a higher frequency and attains higher spatial and temporal resolution. As a result, the reconstructed flow pattern has finer detail and an inflow vortex in early diastole is clearly shown, located on the anterior-posterior plane and below the tricuspid valve. Cardiac flow models by de Vecchi et al. (2012), produced also on HLHS patients, have shown that the abnormal geometry of congenital hearts produces single or multiple intraventricular vortices (similar to the vortex shown in Fig. 16) and the shape and dynamic properties of these vortices have a large effect on cardiac efficiency.

Figure 17 shows a 2D slice of the velocity vectors reconstructed from patient 3 using the proposed method (Fig. 17 (a)) and from 3D+t Flow MRI (Fig. 17 (b)). The projection plane and the frame were manually selected to try to capture the same location and cardiac phase in both images, during diastole where the inflow vortex is larger. It can be observed that the flow pattern (vortex) is similar in both images, with similar velocity distribution, size and location within the ventricle. A portion of the

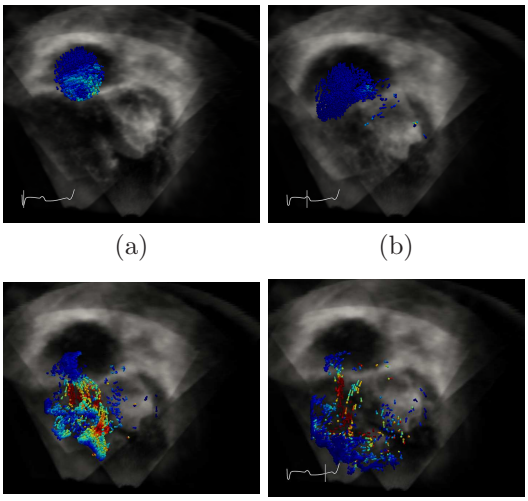

Figure 15: 3D flow reconstructed from HLHS patient 1. Blood motion is represented by particles which follow the velocity field from the right atrium at each time step. The tricuspid valve is initially closed (a), and it opens when atrial pressure overcomes ventricular pressure (b)–(c). After the passive filling, the atrium contracts sending a second jet of blood into the ventricle. Movie 2, showing blood particles tracked over all 24 frames, is provided as additional material.

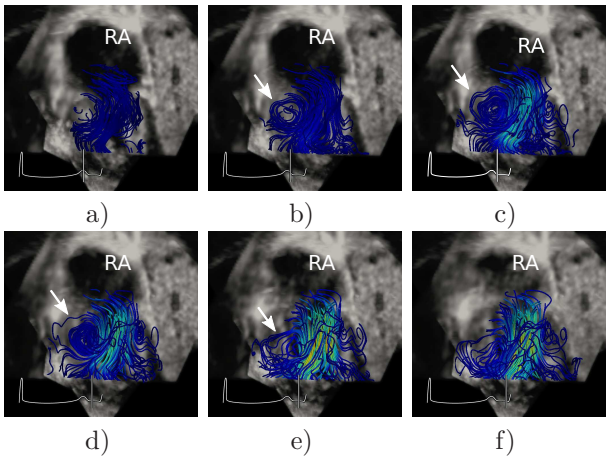

Figure 16: 3D flow reconstructed from HLHS patient 2. The selected frames represent the inflow pattern, including vortex formation in the anterior-posterior plane, below the tricuspid valve, as predicted by cardiovascular models on a similar patient group (de Vecchi et al., 2012). The tricuspid valve is initially closed (a), and it opens when atrial pressure overcomes ventricular pressure (b)–(c). After the passive filling, the atrium contracts sending a second jet of blood into the ventricle. The vortex is indicated with a white arrow.

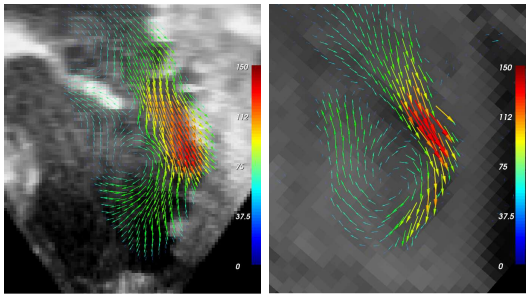

(a) Proposed method. (b) 3D+t Flow MRI.

Figure 17: 2D slice of 3D flow reconstructed from patient 3. Blood motion is represented by arrows which follow the velocity field from the left atrium into the left ventricle. (a) Reconstruction with the proposed method. (b) Reconstruction, in a similar plane, from 3D+t Flow MRI acquired from the same patient less than one hour apart.

ventricle, close to the septum in Fig. 17 (a) lacks of reconstructed data because there was no view overlap. Differences between the two images may be due to differences in projection plane, cardiac phase, patient position and the fact that MRI was acquired over a 10 minute period and echo data over approximately 45 seconds (3 views ×3 images ×5 seconds).

5. Discussion

We have presented a method for 3D velocity reconstruction from multiple 3D colour Doppler views, and a sensitivity analysis to important contributors to inaccuracy. The accuracy of the method has been studied with realistic simulations using a novel noise model that represents realistic variations in colour Doppler images. Our method has been tested on three healthy volunteers and three paediatric patients and compared with the current gold standard technique for non-invasive flow measurements, 2D+t Flow MRI, and when available with 3D+t Flow MRI.

We believe that the major contributors to reconstruction errors are noise in colour Doppler images, view angles and registration errors. The results we

have obtained allow us to propose ranges of these three parameters for which 3D velocity reconstruction will be accurate: 1) registration error has to be TRE$< 2.5mm$, 2) view angles have to be above 20° and 3) noise in colour Doppler images has to be less than $10cm/s$ (table 1).

The extent to which these parameters can be currently achieved with patients requires further investigation. Registration error is difficult to measure on real data without a ground truth, but the similarity measure we use has been reported to provide TRE below $2mm$ (Grau et al., 2007), for which error in flow reconstruction is dominated by the other sources of error: view angles and noise of input data. View angles are limited by patient's anatomy. Our measurements on adult volunteer data (Fig. 11 (a)) show that achieving good angles is not always possible (we only achieved all angles above 20° on one volunteer out of three) and therefore noise in input data must be as low as possible. We believe that further improvement on image quality is required to get the robustness required for clinical practice. The accuracy and the resolution of the reconstructed flow patterns is also limited by the quality and the frequency of the echo probe. Standard adult probes, such as the one used in this paper, are probably not capable of capturing fine flow structures such as small vortices.

Acquisition of sufficiently high quality reproducible Doppler from a wide enough range of angles for our algorithm is challenging on volunteers, and will likely be more challenging on adult patients. Range of angles is anatomically dependent and so will always be an issue, however, methods might be devised which use additional constraints to remove the requirement for three views, as have been achieved by Garcia et al. (2010) who calculated 2D velocities from a single colour Doppler image. In spite of limitations due to noise and view angles, we have successfully reconstructed 3D velocity on a healthy volunteer with an approximate accuracy of 15% showing good quality flow patterns and flow profiles.

Paediatric patients is a patient group which typically has good acoustic windows and provides high quality images. These patients often present complex anatomics (*e.g.* congenital patients) hence more detailed information on cardiac flow could aid diagnosis. In addition, the small size of these patients allows the use of higher frequency probes which may enable the reconstruction of more detailed flow patterns. Our method has been tested on three paediatric patients with an average accuracy of 13.6% and has shown potential for flow pattern reconstruction, including vortices and complex intraventricular filling patterns which agreed well with 3D+t Flow MRI and with predictions from computational models. Further work will include flow reconstruction on a larger set of paediatric patients.

6. Conclusion

We have proposed a scalable patch-wise method to reconstruct realistic 3D blood velocity fields from multiple registered 3D colour Doppler images, and we have identified major contributors to inaccuracy and established the ranges within which flow can be accurately computed.

The advantages of echo over modalities such as MRI in terms of cost and ease of use provides a big impetus to extract additional information from echo. In addition, avoiding general anaesthesia in children is a major attraction of an echo-based method. Our proposed method has potential for quantification of standard blood flow parameters such as stroke volume and blood flood rate, however it also has the potential to provide additional new information such as 3D velocity field visualisation and through-plane velocity profiles, both of which are currently unavailable in echo.

Acknowledgment

The authors would like to thank Irina Waechter-Stehle, Helko Lehmann and Juergen Weese from Philips Healthcare for the help with image conversion.

A.Gomez and D. Giese are founded by the euHeart Project from the European Framework Programme 7.

J. M. Simpson acknowledges financial support from the Department of Health via the National Institute for Health Research award to Guys & St Thomas

NHS Foundation Trust in partnership with Kings College London and Kings College Hospital NHS Foundation Trust.

This research was supported by the National Institute for Health Research (NIHR) Biomedical Research Centre at Guy's and St Thomas' NHS Foundation Trust and King's College London. The views expressed are those of the authors and not necessarily those of the NHS, the NIHR or the Department of Health.

Appendix A. Mathematical Construction of the Linear System

Appendix A.1. General Solution

Let $\mathbf{v}(\mathbf{p}) = [v_x(\mathbf{p})\ v_y(\mathbf{p})\ v_z(\mathbf{p})]^\top$ be the fluid velocity field evaluated at the point $\mathbf{p} = [p_x\ p_y\ p_z]^\top$. We can express $\mathbf{v}(\mathbf{p})$ in the space of uniform B-splines of degree n:

$$v_\gamma(\mathbf{p}) = \sum_{i=1}^{N_g^i}\sum_{j=1}^{N_g^j}\sum_{k=1}^{N_g^k} c^\gamma_{i,j,k}\beta^n_{s,i}(p_x)\beta^n_{s,j}(p_y)\beta^n_{s,k}(p_z) \tag{A.1}$$

where $\gamma \in \{x, y, z\}$, the B-spline grid has a size of $N_g^i \times N_g^j \times N_g^k$, and $\{c^x, c^y, c^z\}_{i,j,k}$ are the B-spline coefficients. Notation for B-Spline functions has been shortened as follows:

$$\beta^n_{s,i}(t) = \beta^n(t/s - i)$$

where $\beta^n(t)$ is the B-spline of degree n and s is the distance between grid nodes and determines the finest resolution of the resulting vector field (*i.e.* its scale).

3D velocity can be reconstructed by extending the method proposed by Arigovindan et al. (2007) to 3D. Each registered view, provides an input Doppler data set $\{m_i, \mathbf{p}_i, \hat{\mathbf{d}}_i\}_{i=1\ldots K}$ where for each point i, m_i is the (projected) velocity measurement at position $\mathbf{p}_i$ where the echo beam direction is $\hat{\mathbf{d}}_i$. Putting all views together, the velocity field $\mathbf{v}$ is the solution to minimising the following energy term

$$J_{proj}(\mathbf{v}) = \sum_k \|\hat{\mathbf{d}}_\mathbf{k} \cdot \mathbf{v}(\mathbf{p}_k) - m_k\|^2 \tag{A.2}$$

The problem can be posed in matrix form by defining the beam matrix (A.3), the coefficient matrix (A.4) and the B-Spline sampling matrix (A.5):

$$\mathbf{D} = [\mathbf{D_x}\ \ \mathbf{D_y}\ \ \mathbf{D_z}]$$
$$\{\mathbf{D_x}\}_{ii} = d_{x,i} \quad \{\mathbf{D_y}\}_{ii} = d_{y,i} \quad \{\mathbf{D_z}\}_{ii} = d_{z,i} \tag{A.3}$$

$$\mathbf{C} = [\mathbf{C_x}\ \ \mathbf{C_y}\ \ \mathbf{C_z}]^\top$$
$$\{\mathbf{C}_\gamma\}_{((i-1)N_g^j+j-1)N_g^k+k,1} = c^\gamma_{i,j,k} \quad \gamma = x, y, z \tag{A.4}$$

$$\mathbf{S} = \begin{bmatrix} \mathbf{S_s} & 0 & 0 \\ 0 & \mathbf{S_s} & 0 \\ 0 & 0 & \mathbf{S_s} \end{bmatrix}$$
$$\{\mathbf{S_s}\}_{r,((i-1)N_g^j+j-1)N_g^k+k} = \beta^n_{s,i}(p_{r,x})\beta^n_{s,j}(p_{r,y})\beta^n_{s,k}(p_{r,z}) \tag{A.5}$$

Equation (A.2) can be expressed in matrix form as follows:

$$\begin{aligned} J_{proj}(\mathbf{C}) &= \|\mathbf{D_x S_s C_x} + \mathbf{D_y S_s C_y} + \mathbf{D_z S_s C_z}\|^2 = \\ &= \|\mathbf{DSC} - \mathbf{m}\|^2 = \\ &= (\mathbf{DSC} - \mathbf{m})^\top(\mathbf{DSC} - \mathbf{m}) \end{aligned} \tag{A.6}$$

where $\mathbf{m} = [m_1 \ldots m_K]^\top$.

Equation (A.6) may be minimised taking the derivative with respect to $\mathbf{C}$, and equating to zero:

$$\begin{aligned} \tfrac{\partial}{\partial \mathbf{C}} J(\mathbf{C}) &= \tfrac{\partial}{\partial \mathbf{C}}\left((\mathbf{DSC})^\top(\mathbf{DSC})\right) - 2\tfrac{\partial}{\partial \mathbf{C}}\left((\mathbf{DSC})^\top\mathbf{m}\right) \\ &= \tfrac{\partial}{\partial \mathbf{C}}\left(\mathbf{C}^\top(\mathbf{DS})^\top(\mathbf{DS})\mathbf{C}\right) - 2\tfrac{\partial}{\partial \mathbf{C}}\left(\mathbf{C}^\top(\mathbf{DS})^\top\mathbf{m}\right) \\ &= 2\mathbf{C}^\top(\mathbf{DS})^\top(\mathbf{DS}) - 2\mathbf{m}^\top(\mathbf{DS}) = 0 \end{aligned} \tag{A.7}$$

$$\begin{aligned} \mathbf{C}^\top &= \mathbf{m}^\top(\mathbf{DS})\left[(\mathbf{DS})^\top(\mathbf{DS})\right]^{-1} \\ \mathbf{C} &= \left[(\mathbf{DS})^\top(\mathbf{DS})\right]^{-1}(\mathbf{DS})^\top\mathbf{m} \\ \mathbf{C} &= \mathbf{A}^{-1}_{proj}\mathbf{b} \end{aligned} \tag{A.8}$$

where $\mathbf{A}_{proj} = \mathbf{S}^\top\mathbf{D}^\top\mathbf{DS}$ and $\mathbf{b} = \mathbf{S}^\top\mathbf{D}^\top\mathbf{m}$. The reconstructed velocity field at the points sampled by $\mathbf{S}$ can be obtained as $\mathbf{V} = \mathbf{SC}$.

Appendix A.2. Incorporation of Physical Constraints

The previously presented linear problem can be regularised by including a divergence penalty term in

the energy function. This kind of regulariser has also been used in 2D by Arigovindan et al. (2007), however the divergence penalty need not necessarily lead to a 2D projection of a 3D incompressible flow. Indeed, Garcia et al. (2010) have proposed to constrain 2D velocity reconstruction to a divergence-free field in 2D, and conclude that this constraint is only valid for certain planes (*e.g.* four chamber) where through plane velocity within the ventricle is almost zero.

Since velocity field is expressed on a B-Spline basis and the derivative of B-Splines can be analytically computed, this constrain can be expressed as a function of B-Spline coefficients. This allows to formulate the problem as a linear matrix equation and is thus solvable by LMS as in the previous section. The new energy function is:

$$J(\mathbf{v}) \quad = \quad (1-\lambda)J_{proj}(\mathbf{v}) + \lambda J_{div}(\mathbf{v})$$

where λ is a weighting factor and

$$J_{div}(\mathbf{v}) = \sum \|\nabla \cdot \mathbf{v}\|^2 \tag{A.9}$$

The right term can be expressed in matrix form. Given that $\nabla \cdot \mathbf{v} = \partial_x v_x + \partial_y v_y + \partial_z v_z$,

$$\partial_x v_x(\mathbf{p}) = \sum_{i=1}^{N_g^i} \sum_{j=1}^{N_g^j} \sum_{k=1}^{N_g^k} c^x_{i,j,k} \dot{\beta}^n_{a,i}(p_x) \beta^n_{a,j}(p_y) \beta^n_{a,k}(p_z) \tag{A.10}$$

where

$$\dot{\beta}^n_{a,l}(\gamma) = \frac{d}{d}\gamma\left(\beta^n_{a,l}(\gamma)\right)$$

and so on for x and z. Then we define the following matrices

$$\{\dot{\mathbf{S}}_x\}_{r,((i-1)N_g^j+j-1)N_g^k+k} = \dot{\beta}^n_{a,i}(p^r_x)\beta^n_{a,j}(p^r_y)\beta^n_{a,k}(p^r_z)$$

$$\{\dot{\mathbf{S}}_y\}_{r,((i-1)N_g^j+j-1)N_g^k+k} = \beta^n_{a,i}(p^r_x)\dot{\beta}^n_{a,j}(p^r_y)\beta^n_{a,k}(p^r_z)$$

$$\{\dot{\mathbf{S}}_z\}_{r,((i-1)N_g^j+j-1)N_g^k+k} = \beta^n_{a,i}(p^r_x)\beta^n_{a,j}(p^r_y)\dot{\beta}^n_{a,k}(p^r_z)$$

Let $\dot{\mathbf{S}} = [\dot{\mathbf{S}}_x\ \dot{\mathbf{S}}_y\ \dot{\mathbf{S}}_z]$, we can write

$$J_{div}(\mathbf{C}) = \dot{\mathbf{S}}\mathbf{C} \tag{A.11}$$

and the full energy term is then

$$J(\mathbf{C}) = (1-\lambda)J_{proj}(\mathbf{C}) + \lambda J_{div}(\mathbf{C}) \tag{A.12}$$

Taking the derivative and equalling to zero yields

$$\begin{aligned} \mathbf{C}^\top\left((1-\lambda)(\mathbf{DS})^\top(\mathbf{DS}) + \lambda\dot{\mathbf{S}}^\top\dot{\mathbf{S}}\right) &= (1-\lambda)(\mathbf{DS})^\top\mathbf{m} \\ \mathbf{C}^\top\mathbf{A} &= (1-\lambda)\mathbf{b} \end{aligned} \tag{A.13}$$

and therefore

$$\mathbf{C} = (1-\lambda)\mathbf{A}^{-1}\mathbf{b} \tag{A.14}$$

where

$$\mathbf{A} = (1-\lambda)\mathbf{A}_{proj} + \lambda\mathbf{A}_{div}$$

Appendix B. Dealiasing of Colour Doppler Images

Although unsupervised de-aliasing methods have been previously investigated, *e.g.* by Muth et al. (2011), aliasing was rarely present in our datasets and therefore manual de-aliasing was an option. First, aliasing borders (*i.e.* the border between aliased and non aliased regions) were detected in each frame by calculating the gradient magnitude of the colour Doppler image and applying a manually tuned threshold using visual inspection. Then a region growing algorithm was used to extract the aliased and non aliased region at each side of each aliasing border. The user would then select which regions were aliased and the selected regions would be unfolded by adding or subtracting twice the velocity range value.

Angelsen, B.A.J., 2000. Ultrasound Imaging: Waves, Signals, and Signal Processing. Emantec, Norway.

Arigovindan, M., Suhling, M., Jansen, C., Hunziker, P., M.Unser, 2007. Full motion and flow field recovery from echo Doppler data. IEEE Trans. Med. Imaging 26, 31–45.

Dunmire, B., Beach, K.W., Labs, K., Plett, M., Strandness, D.E., 2000. Cross-beam vector Doppler ultrasound for angle-independent velocity measurements. Ultrasound Med. Biol. 26, 1213–1235.

Fan, P., Anayiotos, A., Nanda, N., Yoganathan, A., Cape, E., 1994. Intramachine and intermachine

variability in transesophageal color Doppler images of pulsatile jets. in vitro studies. Circulation 89, 2141–2149.

Fitzpatrick, J.M., 2001. Detecting failure, assessing success, in: Hajnal, J.V., Hill, D.L., Hawkes, D.J. (Eds.), Medical Image Registration. CRC Press. chapter 6, pp. 117–139.

Fox, M., 1978. Multiple crossed-beam ultrasound Doppler velocimetry. IEEE Trans. Sonics Ultrason. 25, 281–286.

Garcia, D., del Álamo, J.C., Tanné, D., Yotti, R., Cortina, C., Bertrand, É., Antoranz, J.C., Pérez-David, E., Rieu, R., Fernández-Avilés, F., Bermejo, J., 2010. Two-dimensional intraventricular flow mapping by digital processing conventional color-Doppler echocardiography images. IEEE Trans. Med. Imaging 54, 1167–1178.

Gill, R.W., 1985. Measurement of blood flow by ultrasound: Accuracy and sources of error. Ultrasound Med. Biol. 11, 625–641.

Grau, V., Becher, H., Noble, J.A., 2007. Registration of multiview real-time 3-D echocardiographic sequences. IEEE Trans. Med. Imag. 26, 1154–1165.

Hoskins, P.R., Thrush, A., Martin, K., Wittingham, T. (Eds.), 2010. Diagnostic Ultrasound. Physics and Equipment. Cambridge University Press. 2nd edition.

Maniatis, T.A., Cobbold, R.S., Johnston, K., 1994. Two-dimensional velocity reconstruction strategies for color flow doppler ultrasound images. Ultrasound Med. Biol. 20, 137–145.

Mulet-Parada, M., Noble, J., 2000. 2D+T acoustic boundary detection in echocardiography. Med. Image Anal. 4, 21 – 30.

Muth, S., Dort, S., Sebag, I.A., Blais, M.J., Garcia, D., 2011. Unsupervised dealiasing and denoising of color-doppler data. Medical Image Analysis 15, 577–588.

Pastorelli, A., Torricelli, G., Scabia, M., Biagi, E., Masotti, L., 2008. A real-time 2-d vector doppler system for clinical experimentation. IEEE Trans. Med. Imaging 27, 1515–1524.

Paulsen, P.K., Hasenkam, J.M., 1983. Three-dimensional visualization of velocity profiles in the ascending aorta in dogs, measured with a hot-film anemometer. Journal of Biomechanics 16, 201–210.

Segadal, L., Matre, K., 1987. Blood velocity distribution in the human ascending aorta. Circulation 76, 90–100.

Sengupta, P.P., Pedrizzetti, G., Kilner, P.J., Kheradvar, A., Ebbers, T., Tonti, G., Fraser, A.G., Narula, J., 2012. Emerging trends in CV flow visualization. J. Am. Coll. Cardiol. 5, 305–316.

Tsai-Goodman, B., Geva, T., Odegard, K.C., Sena, L.M., Powell, A.J., 2004. Clinical role, accuracy, and technical aspects of cardiovascular magnetic resonance imaging in infants. Am. J. Cardiol. 94, 69 – 74.

Uejima, T., Koike, A., Sawada, H., Aizawa, T., Ohtsuki, S., Tanaka, M., Furukawa, T., Fraser, A.G., 2010. A new echocardiographic method for identifying vortex flow in the left ventricle: Numerical validation. Ultrasound Med. Biol. 36, 772 – 788.

Unser, M., 1999. Splines: a perfect fit for signal and image processing. IEEE Signal Proc. Mag. 16, 22–38.

de Vecchi, A., Nordsletten, D., Remme, E., Bellsham-Revell, H., Greil, G., Simpson, J., Razavi, R., Smith, N., 2012. Inflow typology and ventricular geometry determine efficiency of filling in the hypoplastic left heart. The Annals of Thoracic Surgery .

Xu, S., Ermert, H., Hammentgen, R., 1991. Phased array pulse Doppler tomography. Proc. IEEE Ultras. Symp. , 1273–1276.

Yao, C., Simpson, J., Schaeffter, T., Penney, G., 2011. Multi-view 3D echocardiography compounding based on feature consistency. Phys. Med. Biol. 56, 6109–6128.